JOM, Vol. 74, No. 4, 2022
https://doi.org/10.1007/s11837-022-05209-z

ENVIRONMENTAL DEGRADATION OF ADDITIVELY MANUFACTURED ALLOYS

Oxidation Resistance in 1200°C Steam of a FeCrAl Alloy Fabricated by Three Metallurgical Processes

ANDREW K. HOFFMAN,[1,2] RAJNIKANT V. UMRETIYA,[1]
VIPUL K. GUPTA,[1] MICHAEL LARSEN,[1] COREY GRAFF,[1]
CHRISTOPHER PERLEE,[1] PATRICK BRENNAN,[1] and RAUL REBAK[1,3]

1.—General Electric Research, Schenectady, NY 12309, USA. 2.—e-mail: Andrew.Hoffman@ge.com. 3.—e-mail: Rebak@ge.com

FeCrAl alloys are a leading candidate material for accident tolerant fuel cladding due to their good performance in both normal light-water reactor operating conditions as well as their resilience to high-temperature accident scenarios. For commercial-scale production, new fabrication techniques need to be investigated. In this study, the effects of fabrication methods on the high-temperature steam oxidation performance of C26M (Fe12Cr6Al2Mo in wt.%) were investigated. Three variants of C26M were manufactured: wrought (cast and forged) (WC26M), powder metallurgy hot isostatic pressing (PMC26M), and laser powder bed fusion additive manufacturing (AMC26M). All three variants were exposed to steam at 1200°C for 2 h. Results showed no significant variation in mass change between the variants after steam exposure. All three variants effectively formed stable protective alumina films with ~0.6–1.3 μm thickness. This study suggests FeCrAl alloys have excellent resilience to high-temperature steam in nuclear reactor accident scenarios regardless of the fabrication method.

INTRODUCTION

In nuclear power generation, fuel elements release energy incessantly through chain nuclear fission, and they are contained in cladding tubes. Thus, the fuel cladding is the first barrier between fuel and coolant, which also plays an important role in preventing the leakage of fission products. Therefore, high reliability and integrity of cladding tubes should be maintained for the safe operation of nuclear reactors. Zr-based alloys have been widely used as fuel cladding in nuclear reactors for a long time because of their low neutron absorbing cross section, good mechanical properties, and high corrosion resistance in normal operation conditions (light water coolant with operating temperatures in the range of 300°C).[1] However, in 2011, the Fukushima accident highlighted weakness of standard Zircaloy cladding, including hydrogen production rate, rapid oxidation at elevated temperatures, and significant heat production from oxidation during high-temperature steam exposure associated with accident scenarios.[2] All these issues led to development of an enhanced accident-tolerant fuel with superior oxidation resistance at high temperatures.[3] The nuclear community is considering two main strategies to develop new fuel technology[4]: (1) application of coatings to Zircaloy cladding and (2) development of non-Zircaloy monolithic alternative materials. A number of studies have demonstrated that ceramic coatings such as SiC,[5] TiAlCrN,[6] and CrN,[7] and metallic coatings such as FeCrAl[8] and Cr[9–12] have excellent resistance to oxidation at higher temperature. Similarly, FeCrAl alloys have shown outstanding high-temperature (≤ 1000°C) oxidation resistance,[13–15] remarkable stability of microstructural and mechanical properties at different radiation doses,[16] and high ultimate tensile and yield strength at different temperatures.[17]

FeCrAl alloys as a lead ATF candidate material can form a protective alumina film during high-temperature steam exposure.[14,18] In addition to their accident tolerance, FeCrAl alloys also exhibit good hydrothermal corrosion behavior because of

---

(Received October 11, 2021; accepted February 3, 2022;

their Cr and Fe content enabling the formation of a protective oxide film.[13,19] Moreover, ferritic alloys tend to have enhanced stress corrosion cracking resistance in nuclear reactor environments compared to austenitic steels or Ni-based alloys.[20]

The manufacture, however, of FeCrAl alloys on a commercial scale can be difficult because of both Cr and Al's decreasing ductility in ferritic alloys.[21,22] Additionally, Al can act to stabilize thermal vacancies in ferritic alloys requiring slow cooling to avoid embrittlement because of trapping of thermal vacancies after casting or high temperature working.[22] Thus, other alternative routes of fabrication are being investigated for commercial production of FeCrAl fuel cladding and structural materials for nuclear reactor applications. Among routes of interest are powder metallurgy methods such as hot isostatic pressing, which does not require slow cooling or hot working to prevent cracking. Additive manufacturing is also of interest to produce near-net-shaped parts. These two methods have yet to be compared, however, to conventional wrought alloys. In this study we compared the accident tolerance of three variants of FeCrAl alloys fabricated using wrought methods (casting and forging), powder metallurgy, and additive manufacturing.

EXPERIMENTAL PROCEDURE

Three variants of C26M were manufactured. The first, wrought C26M (WC26M), was fabricated using conventional casting followed by rotary forging and then stress relief annealing. The second, powder metallurgy C26M (PMC26M), was fabricated by consolidating powders (purchased from Kanthal) using hot isostatic pressing followed by extrusion and stress relief heat treatment. The third, additively manufactured C26M (AMC26M), was fabricated using laser powder bed fusion additive manufacturing followed by a stress relief heat treatment at 800°C for 2 h. Powder used for additive manufacturing was purchased from Oerlikon Metco (US) Inc. and was sieved to a particle size of -45 μm/+15 μm. Samples were printed in a SLM Solutions Single Laser SLM-125 machine. AMC26M samples were sliced perpendicular to the build direction such that the largest exposed surface area plane was normal to the build direction. Table I provides chemical composition of all three types of C26M.

Prior to steam testing, samples were mechanically polished to 600 grit finish and ultrasonically cleaned in de-ionized water and isopropyl alcohol, and weighed. Two samples from each pedigree of C26M (total six samples) were tested. As-manufactured samples were exposed to steam using a high-temperature vertical tube furnace which was purged with argon, brought up to 1200°C, and after reaching the peak temperature high-purity steam was added for 2 h followed by argon purging and gas cooling. Two hours was selected as previous studies have shown that within 2 h FeCrAl alloys will form a stable protective aluminum oxide film, and little additional oxidation occurs.[14,23] It should be noted, however, that slight additional weight gain has been observed after formation of the stable surface oxide.[24] Samples were weighed on an analytical balance (Mettler Toledo XS205) before and after steam exposure, each weight measurement was performed three times, and the average was used for the ultimate weight value. Electron backscatter diffraction (EBSD) was performed on a Hitachi SU-70 FEG-SEM using an Oxford Aztec Symmetry EBSD detector with a 20-kV accelerating voltage, step size of 0.5 μm, and scan area of 1.25×0.94 mm. Transmission electron microscopy (TEM) samples were prepared using focused ion beam (FIB) on an FEI Helios Dual Beam SEM/FIB. TEM was performed using a Tecnai Osiris S/TEM with an accelerating voltage of 200 kV.

RESULTS

Figure 1 shows the microstructures for WC26M and PMC26M with equiaxed grain structures and average grain size of 52.3 ± 21.4 μm and 15.1 ± 1.6 μm, respectively, measured using the average grain intercept method. Figure 2 shows the microstructure of the AMC26M sample, and even after stress relief heat treatment there is a high-volume fraction of low-angle grain boundaries/dislocation cells that formed during fabrication. Additionally, the AMC26M material had some cracks/defects from printing, and future optimization of printing parameters will be used to minimize these fabrication defects.

Mass change and images of WC26M, PMC26M, and AMC26M after exposure to 1200°C steam for 2 h are shown in Fig. 3. Overall, weight gain was between 0.1 mg/cm^2 and 0.2 mg/cm^2. This weight gain is similar to that observed by others for other Fe12Cr6Al alloys.[14,18] This weight gain under high-temperature steam exposure is significantly less than that of zirconium alloys, which have a weight gain on the order of 2 mg/cm^2 under the same conditions.[19] Variation of the AMC26M weight gain compared to PMC26M and WC26M can be attributed to the AM process-induced surface defects (cracks and voids/pores), which could not be accounted for in total surface area measurements.

Figure 4 shows the surface morphology for all three variants of C26M after steam exposure testing. All three surface morphologies differ slightly with the PMC26M alloy showing a flakey texture on top of the uniform Al_2O_3 film. All three alloys form a uniform Al_2O_3 film across the surface of samples with a thickness which varied between ~0.6–1.3 μm. Table II shows the average measured oxide thickness for all three pedigrees of C26M. AMC26M showed the largest variation in oxide thickness, PMC26M showed some variation in oxide thickness, and WC26M showed very uniform thickness in the

Table I. Chemical composition of C26M generated from specimens fabricated by three different metallurgical processing methods

	Elemental concentration (wt.%)						
Material	**Fe**	**Cr**	**Al**	**Mo**	**Y**	**Si**	
WC26M	Bal	11.90	7.00	2.05	0.002	0.13	0.04 Mn, 0.30 Ni
PMC26M	Bal	12.2	5.6	2.02	0.0026	0.025	0.03 Mn, 0.01 Ni
AMC26M	Bal	12.25	5.95	1.99	0.06	0.21	–

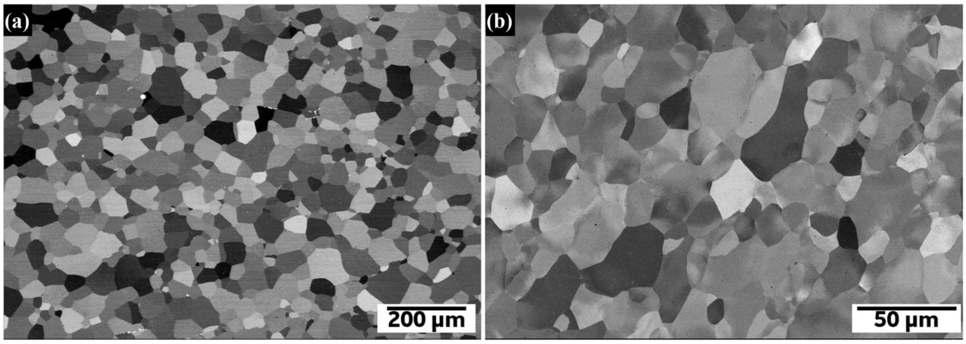

Fig. 1. Microstructure of (a) WC26M and (b) PMC26M.

oxide layer. Interestingly, a unique oxide morphology was found in the AMC26M material (shown in Fig. 4g). This morphology shows a raised structure composed of tetrahedron- and cuboid-shaped crystals, which is atypical for Al_2O_3 oxide formation on FeCrAl alloys. This oxide morphology was found only along fabrication defect cracks (AM defects) with a crack width of ~5–15 μm. Other fabrication defects (such as surface voids/pores) did not form this unique oxide formation.

Figure 5 shows TEM bright-field (BF) and associated energy-dispersion spectroscopy (EDS) maps for WC26M after steam exposure tests. The Al_2O_3 formed is extremely uniform in thickness across the surface, and alumina grains that are formed tend to have a large grain width (> 1 μm). This large grain width can also be observed in Fig. 3a where large grains on the surface of the WC26M are seen. Additionally, Fig. 5 shows that the WC26M forms a very uniform Al_2O_3 oxide layer with only a few Cr oxide particles as seen in Fig. 5f and h. These Cr-enriched particles have also been observed in previous steam oxidation studies of FeCrAl.[14,23–25] No Y-enriched particles were observed in the WC26M shown in Fig. 5.

Figure 6 shows TEM bright-field and associated energy-dispersion spectroscopy (EDS) maps for PMC26M after steam exposure tests. Within the TEM lamella region, the oxide thickness is uniform, but unlike the WC26M the oxide grain structure is refined (< 1 μm) as can be seen in Fig. 6a. This more refined structure is likely influenced by the increased yttrium particle density observed in the PMC26M, which is a consequence of the powder metallurgy process. Small Cr_2O_3 particles are also observed (Fig. 6i) with a similar size and morphology as seen in the WC26M (Fig. 5i.). The bright regions in Fig. 6g are porosity within the oxide layer.

Figure 7 shows TEM BF and associated energy-dispersion spectroscopy (EDS) maps for the uniform Al_2O_3 film formed on AMC26M. Like the PMC26M, the AMC26M alumina has a more refined grain structure though not to the extent as that seen in PMC26M. This is also likely due to the amount of Y_2O_3 particles as observed in Fig. 7j. The yttrium content in AMC26M is significantly higher than that of PMC26M, so the reason for increased Y2O3 content in the PMC26M compared to the AMC26M still remains to be investigated.

Figure 8 shows TEM BF and associated EDS chemical maps for the oxides formed along the cross section of an AM defect crack in AMC26M. Interestingly the "ridged" structure shown in Fig. 4g is explained through the TEM results in Fig. 8 with the tetrahedron and cuboid oxide crystals showing the formation of Cr_2O_3. Additionally, the formation of Si oxide is also observed. Interestingly, along the transition region, the Cr_2O_3 forms on top of the Al_2O_3. The Cr_2O_3 also forms within the crack itself in addition to the ridged region observed in Fig. 4g.

DISCUSSION

There are many studies on oxidation behavior of FeCrAl alloys after high-temperature air and steam exposure showing excellent performance due to

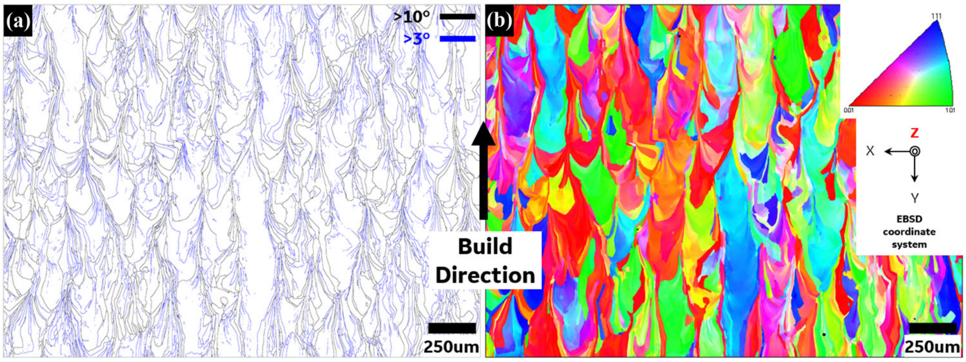

Fig. 2. EBSD maps of AMC26M before steam exposure showing (a) the grain boundary misorientation map and (b) the inverse pole figure with respect to the z-direction as annotated.

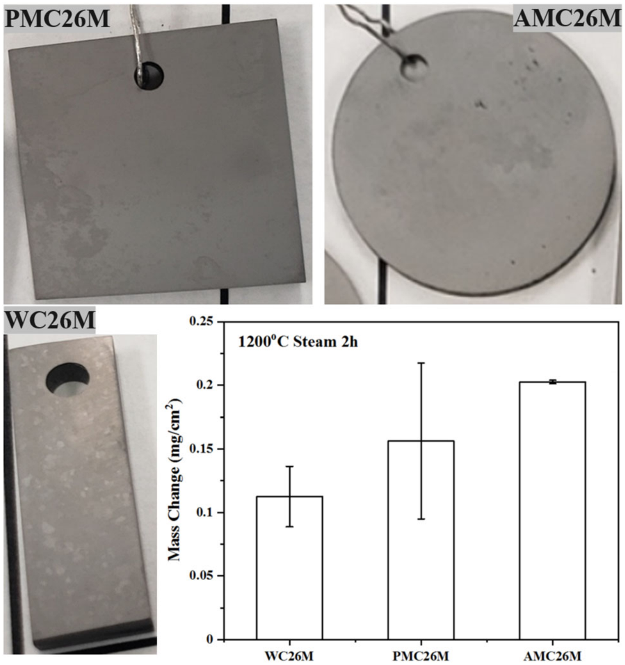

Fig. 3. Images of WC26M, PMC26M, and AMC26M with weight gain comparison of all three C26M variants after 2 h steam exposure at 1200°C.

protective Al oxide film formation at temperatures $> 600°C$.[24–31] However, there are limited studies on FeCrAl alloys produced using additive manufacturing.[32] Additionally, few comparisons of manufacturing route on high-temperature oxidation behavior of FeCrAl alloys have been performed. In this study the three manufacturing variants WC26M, PMC26M, and AMC26M exhibit very similar behavior in both weight gain and oxide morphology. This agrees with the previous study by Gunduz et al. of high-temperature oxidation of additively manufactured FeCrAl alloys in dry air.[32]

First, the AMC26M material showed slightly higher weight gain compared to the wrought and powder metallurgy alloys. This difference could be due to slight differences in chemistry and microstructure as Fe and Cr can play a role in the oxidation mechanism of FeCrAl and the kinetics of α-Al_2O_3 establishment.[33,34] Compositionally, Cr in particular has a large beneficial effect on promoting the establishment of α-Al_2O_3. This typically attributed to a “template” effect[35,36] because α-Cr_2O_3 shares the same rhombohedral structure α-Al_2O_3. It is thought that the formation of α-Cr_2O_3 in the transient stages of oxidation and encourages the formation of α-Al_2O_3 opposed to metastable forms of alumina. Additionally, there is some evidence that the presence of Cr can enhance Al diffusion to the oxidation front in the early stages of FeCrAl oxidation by increasing the chemical potential gradient for Al diffusion in the alloy substrate.[37,38] It should be noted, however, that minor chemistry changes in alloy composition are only expected to alter the kinetics of α-Al_2O_3 establishment as the oxidation of Al to Al_2O_3 has the highest priority in this environment.[33] The difference in weight gain of the AMC26M alloy could also be due to either unaccounted increased surface area due to small fabrication defects or the formation of Cr_2O_3 ridges along AM defects.

Second, the oxide film thickness varied the most in the AMC26M alloy. A similar behavior was observed in additively manufactured Fe21Cr5.5Al oxidized in dry air at 900°C and 1100°C. Gunduz et al. showed in the study that these differences in film thickness were linked to the crystallographic orientation of the grains.[32] Although in this study only one primary surface (the surface normal to the build direction) was examined, future studies should be done to investigate the effect of texture on steam oxidation. Gunduz also noted that at 1100°C microstructure effects on the overall oxidation behavior are less pronounced as the kinetics are rapid at 1100°C. In this study, we expect kinetics to be even faster at 1200°C in a steam environment than that experienced in air at 1100°C. Although the AMC26M alloy did still contain a microstructure with a high-volume fraction of low-angle grain boundaries (as seen in Fig. 2), there is no evidence of oxide ridges forming in Fig. 4e. This consequently has been attributed to the rapid kinetics at 1200°C in this study. TEM also did not show any signs of ridges or inhomogeneous chemistry within the

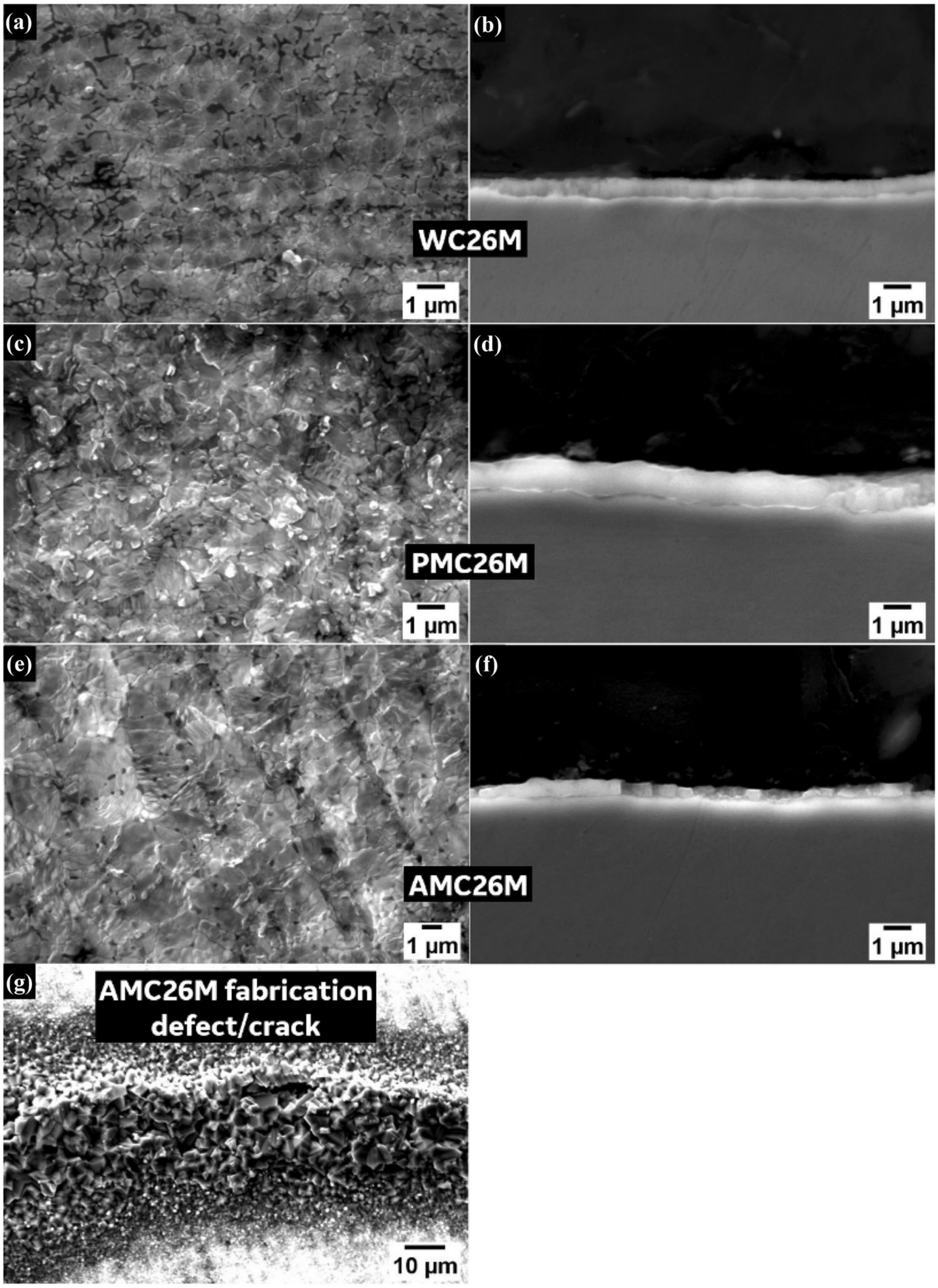

Fig. 4. SEM secondary electron images for surface morphology and cross sections of the protective Al_2O_3 film for WC26M (a–b), PMC26M (c–d), and AMC26M (e–f). (g) SEM of unique oxide formation along AM defects in AMC26M.

Table II. Average oxide thickness of WC26M, PMC26M, and AMC26M after steam exposure for 2 h at 1200°C

Sample	Oxide thickness
WC26M	$1.04 \pm 0.11\ \mu m$
PMC26M	$1.13 \pm 0.20\ \mu m$
AMC26M	$0.86 \pm 0.24\ \mu m$

surface oxide layer aside from small Y_2O_3 particles. Although we did not observe ridges, the low angle grain boundaries could still act as effective diffusion channels for enhanced passivation within a localized region contributing to local differences in the passive layer oxide.[39]

Third, the AMC26M material showed extremely unique behavior in the fabrication defect cracks. The formation of Cr_2O_3 ridges on and within the cracks is contradictory to expected behavior as Cr_2O_3 will evaporate in high-temperature steam environments.[40] Although the authors cannot

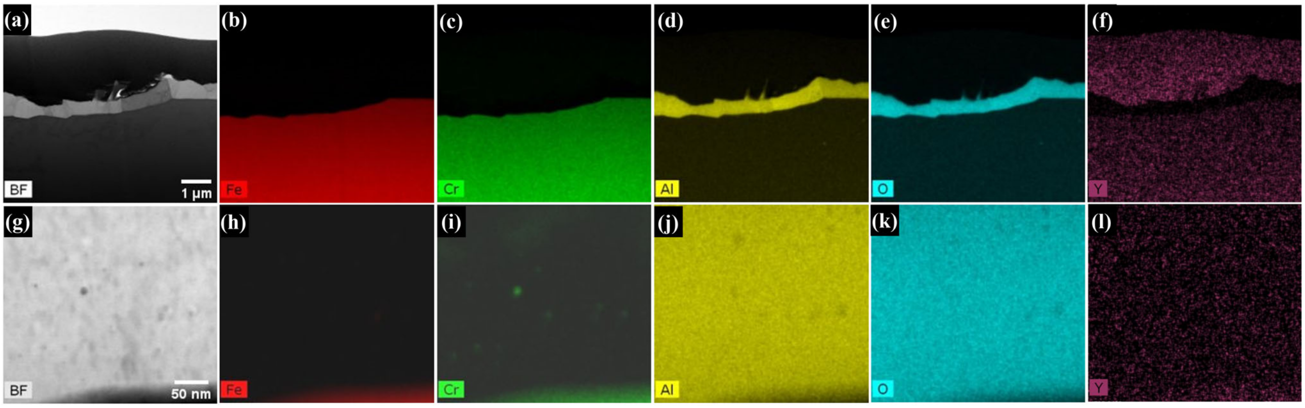

Fig. 5. (a,g) TEM BF of WC26M with (b–f) and (h–l) showing associated EDS chemical maps.

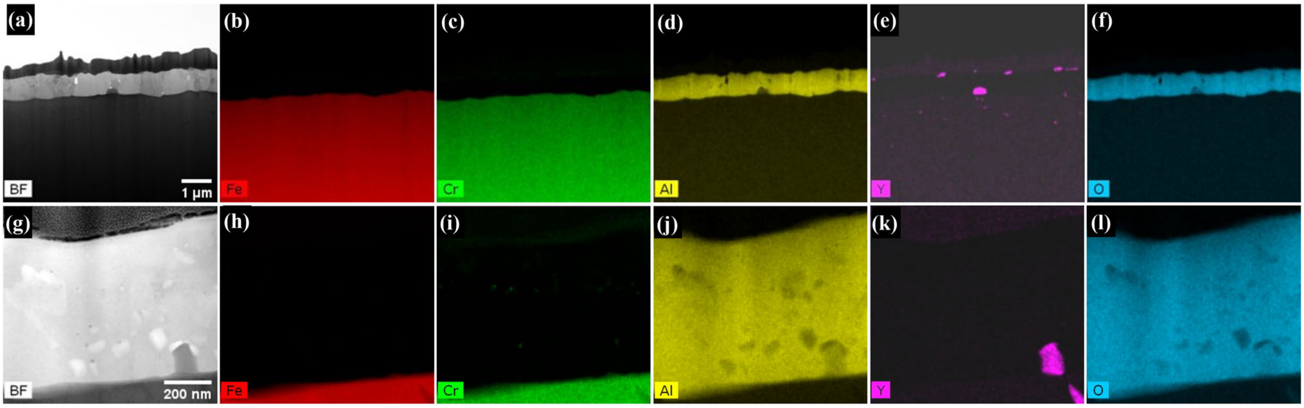

Fig. 6. (a) and (g) TEM BF of PMC26M with (b–f) and (h–l) showing associated EDS chemical maps.

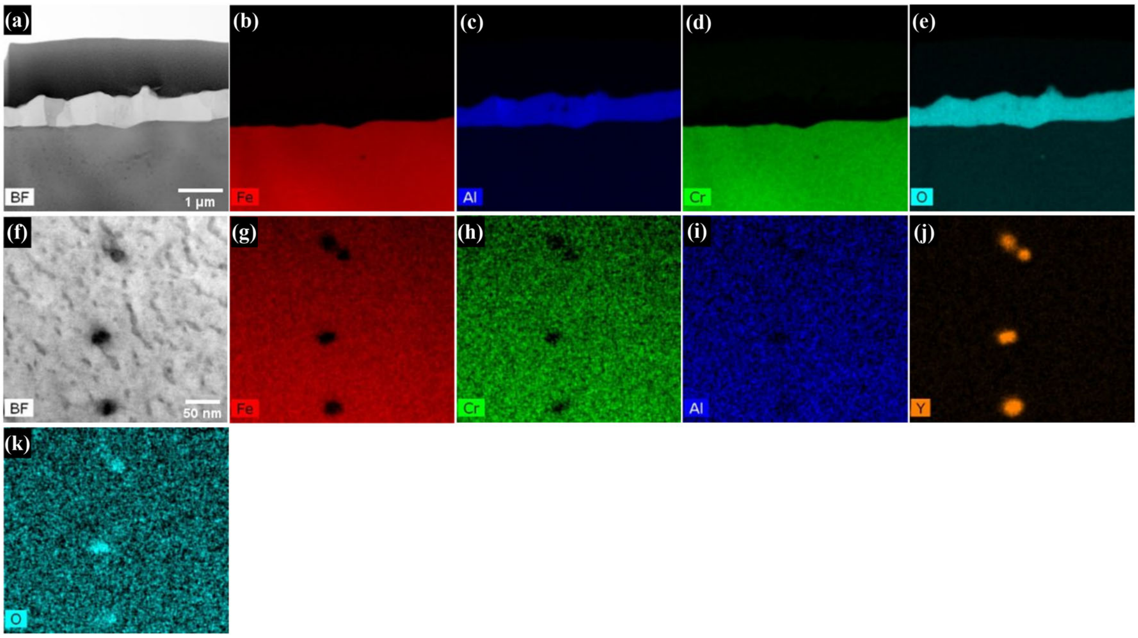

Fig. 7. (a) and (f) TEM BF of AMC26M with (b–e) and (g–k) showing associated EDS chemical maps.

currently provide an explanation for this behavior, it provides an interesting topic of investigation for the community to study the impact of AM process defects on high-temperature corrosion behavior.

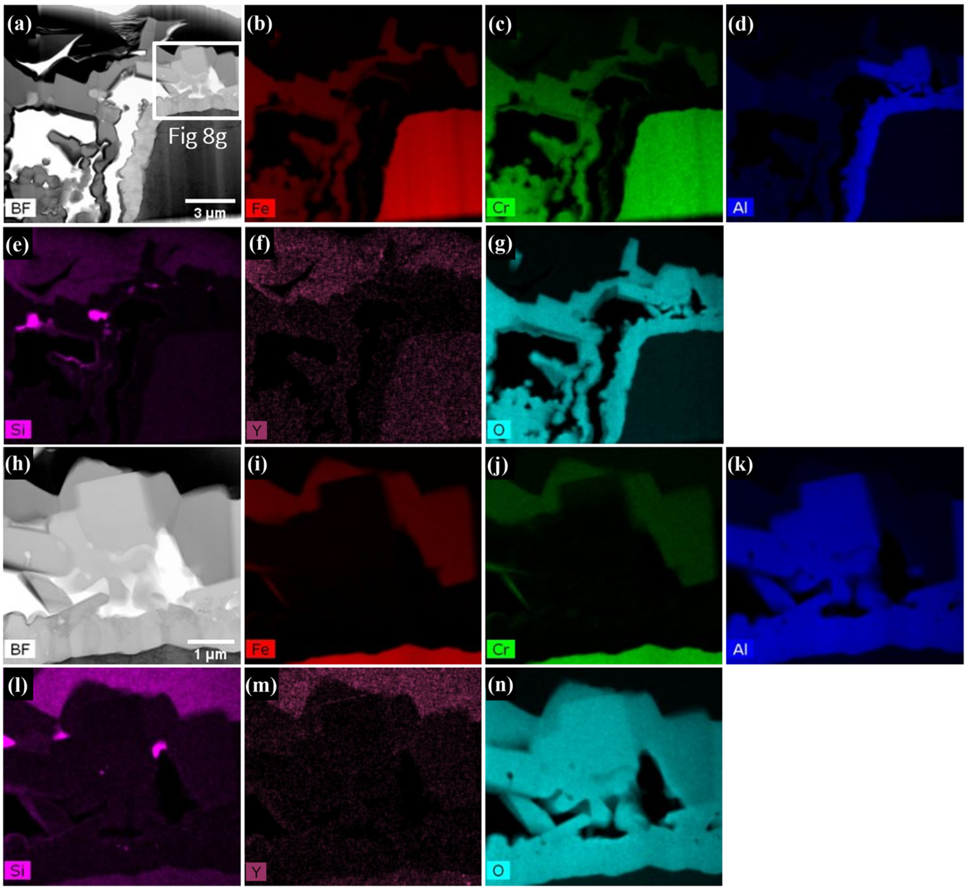

Fig. 8. (a) and (h) TEM BF image of AMC26M (structure shown in Fig 4g) with (b–g) and (h–n) showing associated EDS chemical maps.

From an applications standpoint, the Cr_2O_3 ridges along cracks can be avoided through optimization of build parameters for future manufacturing of AMC26M and thus are expected to have little impact on commercial applications of additive FeCrAl alloys.

CONCLUSION

Three variants of C26M (wrought, powder metallurgy, and additively manufactured) were exposed to steam at 1200°C for 2 h. After steam exposure all samples showed similar weight gain. Protective alumina films formed on all three fabrication variants with a similar thickness of 0.6–1.3 μm. Surface morphologies of the alumina films were also similar among all three variants. Interestingly, fabrication defects within the AMC26M sample showed unique formation of chromia within the defects causing a ridged oxide morphology along AM defects. Overall, it can be concluded that FeCrAl alloy high-temperature steam oxidation resistance has little sensitivity to microstructural impacts of the fabrication route.

ACKNOWLEDGEMENTS

The financial support of Global Nuclear Fuel Americas, GE Hitachi Nuclear Energy, and GE Research is gratefully acknowledged. The contributions of Ian Spinelli (EBSD), Steve Buresh (sample fabrication), Sharon Huang (metallurgy and sample fabrication), and Evan Dolley (metallurgy and sample fabrication) are as also gratefully acknowledged. This material is based upon work supported by the Department of Energy (National Nuclear Security Administration) under award no. DE-NE0008823.

CONFLICT OF INTEREST

On behalf of all authors, the corresponding author states that there is no conflict of interest.

OPEN ACCESS

REFERENCES

1. R.B. Rebak, *Accident Tolerant Materials for Light Water Reactor Fuels* (Elsevier, Amsterdam, 2020).
2. I.A.E.A., The Fukushima Daiichi Accident Report by the Director General, Dir. Gen. (2015) 1–222.
3. S.J. Zinkle, K.A. Terrani, J.C. Gehin, L.J. Ott, and L.L. Snead, *J. Nucl. Mater.* 448, 374 (2014).
4. F. Goldner, OECD/ NEA Work. 14 (2013).
5. K. Lee, D. Kim, and Y.S. Yoon, *Thin Solid Films* 660, 221 (2018).
6. X.F. Ma, Y.W. Wu, J. Tan, C.Y. Meng, L. Yang, W.A. Dang, and X.J. He, *Surf. Coat. Technol.* 358, 521 (2019).
7. C. Meng, L. Yang, Y. Wu, J. Tan, W. Dang, X. He, and X. Ma, *J. Nucl. Mater.* 515, 354 (2019).
8. T. Dabney, G. Johnson, H. Yeom, B. Maier, J. Walters, and K. Sridharan, *Nucl. Mater. Energy* 21, 100715 (2019).
9. V.N. Voyevodin, A.S. Kuprin, E.N. Reshetnyak, V.D. Ovcharenko, R.L. Vasilenko, V.V. Bryk, V.A. Belous, P.N. V'yugov, and G.N. Tolmachova, *J. Nucl. Mater.* 465, 400 (2015).
10. H.G. Kim, I.H. Kim, Y. Il Jung, D.J. Park, J.Y. Park, and Y.H. Koo, *J. Nucl. Mater.* 465, 531 (2015).
11. H.-G. Kim, Y.-I. Jung, J.-H. Park, D.-J. Park, Y.-H. Koo, and J. Park, *Surf. Coat. Technol.* 280, 256 (2015).
12. R.V. Umretiya, B. Elward, D. Lee, M. Anderson, R.B. Rebak, and J.V. Rojas, *J. Nucl. Mater.* 541, 50 (2020).
13. S.S. Raiman, K.G. Field, R.B. Rebak, Y. Yamamoto, and K.A. Terrani, *J. Nucl. Mater.* 536, 152221 (2020).
14. R.B. Rebak, V.K. Gupta, and M. Larsen, *JOM* 70, 1484. (2018).
15. B. A. Pint, K. A. Terrani, and R. B. Rebak, Miner. Met. Mater. Ser. 1451 (2019).
16. E. Aydogan, J.S. Weaver, S.A. Maloy, O. El-Atwani, Y.Q. Wang, and N.A. Mara, *J. Nucl. Mater.* 503, 250 (2018).
17. Y. He, J. Liu, S. Qiu, Z. Deng, Y. Yang, and A. McLean, *Mater. Sci. Eng. A* 726, 56 (2018).
18. K. Lipkina, D. Hallatt, E. Geiger, B.W.N. Fitzpatrick, K. Sakamoto, H. Shibata, and M.H.A. Piro, *J. Nucl. Mater.* 541, 152305 (2020).
19. D.J. Park, H.G. Kim, J.Y. Park, Y. Il Jung, J.H. Park, and Y.H. Koo, *Corros. Sci.* 94, 459 (2015).
20. S.J. Zinkle and G.S. Was, *Acta Mater.* 61, 735 (2013).
21. M. Matijasevic and A. Almazouzi, *J. Nucl. Mater.* 377, 147 (2008).
22. J. Herrmann, G. Inden, and G. Sauthoff, *Acta Mater.* 51, 2847 (2003).
23. R. B. Rebak, R. J. Blair, P. J. Martiniano, F. Wagenbaugh, and E. J. Dolley, in NACE - Int. Corros. Conf. Ser. (2014), pp. 1–14.
24. K.A. Unocic, Y. Yamamoto, and B.A. Pint, *Oxid. Met.* 87, 431 (2017).
25. B.A. Pint, K.A. Unocic, and K.A. Terrani, *Mater. High Temp.* 32, 28 (2015).
26. C. Badini and F. Laurella, *Surf. Coat. Technol.* 135, 291. (2001).
27. S. Canovic, J. Engkvist, F. Liu, H. Lai, H. Götlind, K. Hellström, J.-E. Svensson, L.-G. Johansson, M. Olsson, and M. Halvarsson, *J. Electrochem. Soc.* 157, C223 (2010).
28. R. Cueff, H. Buscail, E. Caudron, C. Issartel, and F. Riffard, *Oxid. Met.* 58, 439 (2002).
29. N. Li, S.S. Parker, E.S. Wood, and A.T. Nelson, *Metall. Mater. Trans. A* 49, 2940 (2018).
30. H. Josefsson, F. Liu, J.-E. Svensson, M. Halvarsson, and L.-G. Johansson, *Mater. Corros.* 56, 801 (2005).
31. J. Engkvist, U. Bexell, M. Grehk, and M. Olsson, *Mater. Corros.* 60, 876 (2009).
32. K.O. Gunduz, A. Visibile, M. Sattari, I. Fedorova, S. Saleem, K. Stiller, M. Halvarsson, and J. Froitzheim, *Corros. Sci.* 188, 109553 (2021).
33. Y. Qiao, P. Wang, W. Qi, S. Du, Z. Liu, F. Meng, X. Zhang, K. Wang, Q. Li, Z. Yao, C. Bai, and X.D. Wang, *J. Alloys Compd.* 828, 154310 (2020).
34. P. Tomaszewicz and G.R. Wallwork, *Corrosion* 40, 152 (1984).
35. Y. Kitajima, S. Hayashi, T. Nishimoto, T. Narita, and S. Ukai, *Oxid. Met.* 75, 41 (2011).
36. Y. Kitajima, S. Hayashi, T. Nishimoto, T. Narita, and S. Ukai, *Oxid. Met.* 73, 375 (2010).
37. M.H. Heinonen, K. Kokko, M.P.J. Punkkinen, E. Nurmi, J. Kollár, and L. Vitos, *Oxid. Met.* 76, 331 (2011).
38. E. Airiskallio, E. Nurmi, M.H. Heinonen, I.J. Väyrynen, K. Kokko, M. Ropo, M.P.J. Punkkinen, H. Pitkänen, M. Alatalo, J. Kollár, B. Johansson, and L. Vitos, *Corros. Sci.* 52, 3394 (2010).
39. V. S. Saji, in *Corrosion Protection and Control Using Nanomaterials* (2012), pp. 3–15.
40. A. Yamauchi, K. Kurokawa, and H. Takahashi, *Oxid. Met.* 59, 517 (2003).